Journal of Materials Chemistry C

PAPER

View Article Online
View Journal | View Issue

Cite this: J. Mater. Chem. C, 2019, 7, 14594

Aliovalent substitution toward reinforced structural rigidity in Ce^{3+}-doped garnet phosphors featuring improved performance†

Tao Hu,[a] Maxim S. Molokeev,[bcd] Zhiguo Xia *[a] and Qinyuan Zhang *[a]

Received 29th September 2019,
Accepted 28th October 2019

DOI: 10.1039/c9tc05354a

rsc.li/materials-c

Highly efficient phosphors with thermal stability and color-tunable emission are required for the fabrication of phosphor-converted white light-emitting diodes (pc-WLEDs). Currently developed engineering strategies are generally successful in photoluminescence tuning but, unfortunately, suffer severe deterioration in emission intensity/efficiency and/or thermal stability. Herein, an efficient aliovalent substitution strategy toward reinforced structural rigidity is proposed and demonstrated experimentally. By incorporating Be^{2+} ion into the garnet-type $Lu_2SrAl_4SiO_{12}:Ce^{3+}$ phosphor, the phosphor shows enhanced internal/external quantum efficiency, from 79.2%/26.7% to 84.5%/32.9%, photoluminescence tuning from green (peaking at ~512 nm) to yellow (peaking at ~552 nm), and zero thermal quenching, even up to 200 °C. The Be^{2+} substitution at the Al_2/Si_2 site enables stable and rigid local surroundings around the Ce^{3+} activator, which is responsible for the unprecedented performance. In addition, high-quality warm WLED devices with a luminous efficiency of 158.1 lm W^{-1}, correlated color temperature of 3858 K and high color rendering index of 81.7, are obtained by combining $Lu_2SrAl_4SiO_{12}:Ce^{3+},Be^{2+}$ as the yellow emitter, $CaAlSiN_3:Eu^{2+}$ as the red emitter and a blue-emitting InGaN chip. These findings highlight a new strategy for performance optimization of LED phosphors by selecting rigid covalent compounds with further reinforced structural rigidity *via* aliovalent substitution.

1. Introduction

Phosphor-converted white light-emitting diodes (pc-WLEDs) have become extensively integrated into the global lighting market and will definitely replace compact fluorescent and incandescent lamps, due to their energy saving, high luminous efficacy, long lifetime and environmentally friendly features.[1–5] To target pc-WLEDs with specific photoluminescence properties, phosphors with various emission characteristics have been investigated.[6,7] In particular, highly efficient phosphors with thermally stable luminescence for high-performance WLEDs is highly desirable.[8,9] Therefore, promotion of these luminescent properties of phosphors is essential to fulfill the needs of versatile applications. Currently, many strategies, including cationic/anionic substitution, crystal-site engineering approaches, and the selection of energy transfer couples, *etc.*, have been proposed to engineer the luminescence properties of phosphors.[10–12] Nevertheless, there are still several issues to be addressed. For example, photoluminescence tuning may be achieved by seriously sacrificing other features, such as efficiency or thermal stability,[13,14] which results in a lowered luminous efficiency and altered white balance of the pc-WLEDs. Therefore, rational design of phosphors for improved performance remains a big challenge.

Understanding their structure–property relationships allows us to discover phosphors with unprecedented properties, and to further expand the applications of state-of-the-art pc-WLEDs. Thus, it is well established that a phosphor host with a rigid crystal structure is likely to have high efficiency luminescence, since the non-radiative relaxation probability is inhibited.[15–17] The structural rigidity is not only associated with the degree of dense connectivity of the crystal, but also with internal chemical bond strength,[18] as pointed out by Brgoch *et al.* Thus, a better-connected three-dimensional network and stronger bond interactions tend to form a more rigid structure.[18,19] Following on from this, many efficient phosphors have been identified recently.[20] According to Pauling's radius ratio rule, Be^{2+} often dominates in the BeO_4 tetrahedron.[21] As for the Be–O bond energy, this is estimated by Pauling's ionic character $I = 1 - \exp(-\Delta\chi^2/4)$ ($\Delta\chi$, Pauling electronegativity difference) and has a value of 0.58 (SiO_2: 0.45), indicating that Be–O has a strong

[a] State Key Laboratory of Luminescent Materials and Devices and Institute of Optical Communication Materials, South China University of Technology, Guangzhou 510641, China. E-mail: xiazg@scut.edu.cn, qyzhang@scut.edu.cn
[b] Laboratory of Crystal Physics, Kirensky Institute of Physics, Federal Research Center KSC SB RAS, Krasnoyarsk 660036, Russia
[c] Siberian Federal University, Krasnoyarsk 660041, Russia
[d] Department of Physics, Far Eastern State Transport University, Khabarovsk 680021, Russia

† Electronic supplementary information (ESI) available. See DOI: 10.1039/c9tc05354a

covalent character.[22] Moreover, Be-containing compounds are likely to have an extremely condensed network with a degree of condensation of $k \geq 1$. For example, k is expected to reach values to 1 in BeO and 1.5 in Be_3N_2, which makes Be-containing compounds of interest for developing highly efficient phosphors. In fact, this was verified recently with the high efficiency oxo- and nitridoberyllates $AELi_2[Be_4O_6]:Eu^{2+}$ (AE = Sr, Ba), $SrBeO_2:Eu^{2+}$, $Sr[Be_6ON_4]:Eu^{2+}$ and $MBe_{20}N_{14}:Eu^{2+}$ (M = Sr, Ba) phosphors.[23–26] Based on these considerations, it seems that chemical incorporation of tetrahedral Be^{2+} into a phosphor host may potentially optimize the optical performance, as expected.

In this work, we propose, and demonstrate experimentally, a new way to prepare a Ce^{3+}-doped aluminosilicate-based garnet phosphor by substitutionally incorporating Be^{2+} ions into tetrahedral coordinated Al/Si sites for the first time. For a typical example of a garnet phosphor, $Lu_2SrAl_4SiO_{12}:Ce^{3+}$ (hereafter abbreviated as LSAS:Ce), we find that, as predicted, its emission intensity increases and, accordingly, its quantum efficiency is enhanced upon Be^{2+} doping, thanks to the suppressed non-radiative relaxation probability. Moreover, emission colors can also be facilely tuned from green to yellow and the thermal quenching temperature remains extraordinarily high. Investigations were first performed to elucidate the observed phenomenon caused by Be^{2+}. Furthermore, the optical properties of fabricated WLED devices with enhanced performance were studied. Our work provides a new method for photoluminescence tuning and performance optimization of WLED phosphors *via* aliovalent substitution, with reinforced local structural rigidity.

2. Synthesis and characterization

Synthesis

$Lu_2SrAl_4SiO_{12}:0.06Ce,xBe$ (x = 0.00–0.50) was synthesized by the high-temperature solid-state method using Lu_2O_3 (99.99%), $SrCO_3$ (99.99%), Al_2O_3 (99.99%), SiO_2 (99.99%), CeO_2 (99.99%), and BeO (99.9%) as starting materials. Note that the BeO is of low toxicity, to reduce the risk of exposure, and the raw materials were weighed and ground thoroughly in a closed glove box. The mixtures were sintered under a reducing atmosphere (10% H_2 + 90% N_2) at 1400 °C for 4 h to obtain the final products. The final samples containing the element Be were safe for analysis and application due to their low percentage content.

Characterization

Powder X-ray diffraction (XRD) measurements were performed on an Aeris X-ray diffractometer (PANalytical Corporation, The Netherlands) operating at 40 kV and 15 mA with monochromatized CuKα radiation (λ = 1.5406 Å). The Rietveld structure refinements were performed using TOPAS 4.2.[27] Photoluminescence (PL), photoluminescence excitation (PLE) and temperature-dependent luminescence spectra were recorded using a Hitachi F-4600 fluorescence spectrophotometer. The luminescent decay curves were measured using an Edinburgh FLS920 fluorescence spectrophotometer equipped with an nF900 flash lamp. The photoluminescence quantum yields (PLQYs) were recorded using a commercialized PLQY measurement system from Ocean Optics, with 450 nm light excitation. The photoluminescence spectra, luminous efficacy (LE), color-rendering index (R_a), and correlated color temperature (CCT) of the fabricated WLEDs were measured using an integrating sphere of 1.0 m diameter connected to a CCD detector.

3. Results and discussion

As a consequence of the strong metal–ligand bonding characteristics of the Be–O bond mentioned above, we propose that the structural rigidity can be optimized so that the luminescent properties depend on the Be^{2+} doping. From screening of the systems studied, it is known that the absorption of the Ce^{3+} ion in garnet phosphors is located in the blue region of the spectrum, which matches well with the emission of the InGaN blue chip. Moreover, the lattice of garnet-type compounds offers remarkable flexibility for structural modification and photoluminescence tuning due to its ability to accommodate various cations. Thus, in the present case, the tetrahedral coordinated sites can hopefully be substituted by Be^{2+} ions. Therefore, we carried out a proof-of-concept experiment on a Ce^{3+}-doped garnet prototype system, since it has attracted much attention among the WLED phosphor families.[28–30]

As an embodiment of LSAS garnet, the phosphor crystallizes in a body-centered cubic structure (space group $Ia\bar{3}d$) with three-dimensional framework formed by edge- and vertex-shared Lu/SrO_8 dodecahedra (Wyck. 24c), $Al1O_6$ octahedra (Wyck. 16a), and Al_2/Si_2O_4 tetrahedra (Wyck. 24d), as shown in Fig. 1a. The Ce^{3+} ion occupies the Lu/Sr site, while Al_2/Si_2O_4 tetrahedral site is potentially available for Be^{2+} doping, as discussed below. As a consequence, Ce^{3+} ions experience a more stable and rigid local environment. Fig. 1b gives the XRD patterns of LSAS:Ce,xBe (x = 0.00, 0.10, 0.20 and 0.40) with almost all peaks indexed to the cubic cell ($Ia\bar{3}d$) and with cell parameters close to the garnet-type structure $Y_3Al_5O_{12}$.[31] In the meantime, we find that the characteristic diffraction peak (0 2 4) shifts to higher diffraction angles from 33.53° to 33.92°, in agreement with increasing Be^{2+} doping concentration and the induced decrease in cell parameters. To further analyze the local structures of the as-synthesized samples, Rietveld refinements were performed taking $Y_3Al_5O_{12}$ as the starting model. The site of the Y ion was occupied by Lu/Sr/Ce ions with fixed occupations according to the suggested formula. One Al site with octahedral coordination was occupied by the Al ion only, but a second site with tetrahedral coordination was occupied by Al/Si/Be ions according to the chemical formula. Refinements were stable and gave low R-factors (Fig. S1 and Table S1, ESI†). The coordinates of the atoms and main bond lengths are listed in Tables S2 and S3 (ESI†), respectively, and the crystallographic information files for these four samples are presented in the ESI.† Furthermore, the decreasing trend of cell volume $V(x)$ and cell parameter a (Fig. 1c, and inset) further proves successful Be^{2+} doping in the host. Moreover, the average bond length $d(Al_2/Si_2/Be_2–O)$ noticeably decreased with increasing x(Be) (Fig. 2d), and the calculated $Al_2/Si_2/Be_2–O$ average bond length

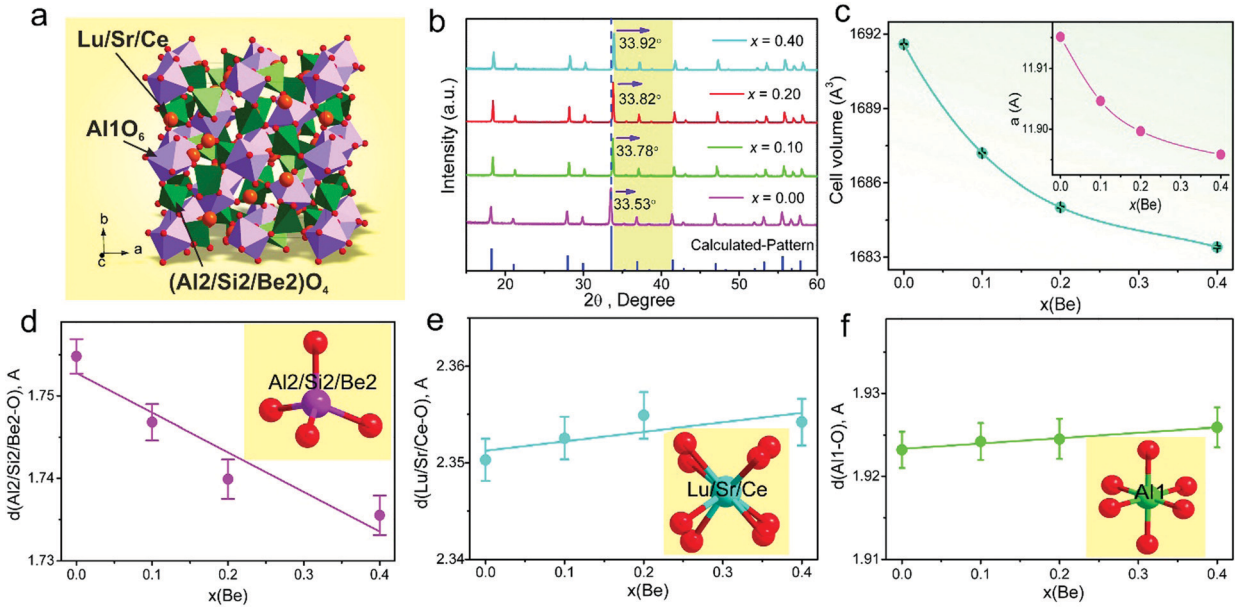

Fig. 1 (a) The unit cell of LSAS:Ce,*x*Be showing polyhedrons of $Al1O_6$ octahedra (pink) and $Al_2/Si_2/Be_2O_4$ tetrahedra (green), Ce^{3+} ions replace Lu/Sr ions in one site. (b) Measured X-ray patterns of LSAS:Ce,*x*Be compounds and the calculated pattern based on Rietveld refinement. The dotted blue line and purple arrows are drawn as a guide of the patterns move to high the 2θ side along with increasing Be^{2+} concentration, *x*. The dependencies per *x*(Be) of (c) cell volume *V*(*x*), cell parameter *a* (inset 2c), (d) average bond length *d*($Al_2/Si_2/Be_2$–O), (e) average bond length *d*(Lu/Sr/Ce–O), and (f) average bond length *d*(Al1–O) in LSAS:Ce,*x*Be compounds.

of ~1.7 Å is in accordance with the Be–O distance (1.65 Å) reported in the literature.[32] All other bond lengths remain almost unchanged within one estimated standard deviation, σ (Fig. 2e and f), so one can suggest that the Be^{2+} doping substitutes preferably at the Al_2/Si_2 site. The reason for such a mechanism can be understood by comparing the smaller tetrahedral Al_2/Si_2 site with the Al1 octahedral site and the Lu/SrO_8 dodecahedral site, with only this small site being preferable for the small Be^{2+} ion. Be^{2+} at the tetrahedral Al_2/Si_2 site

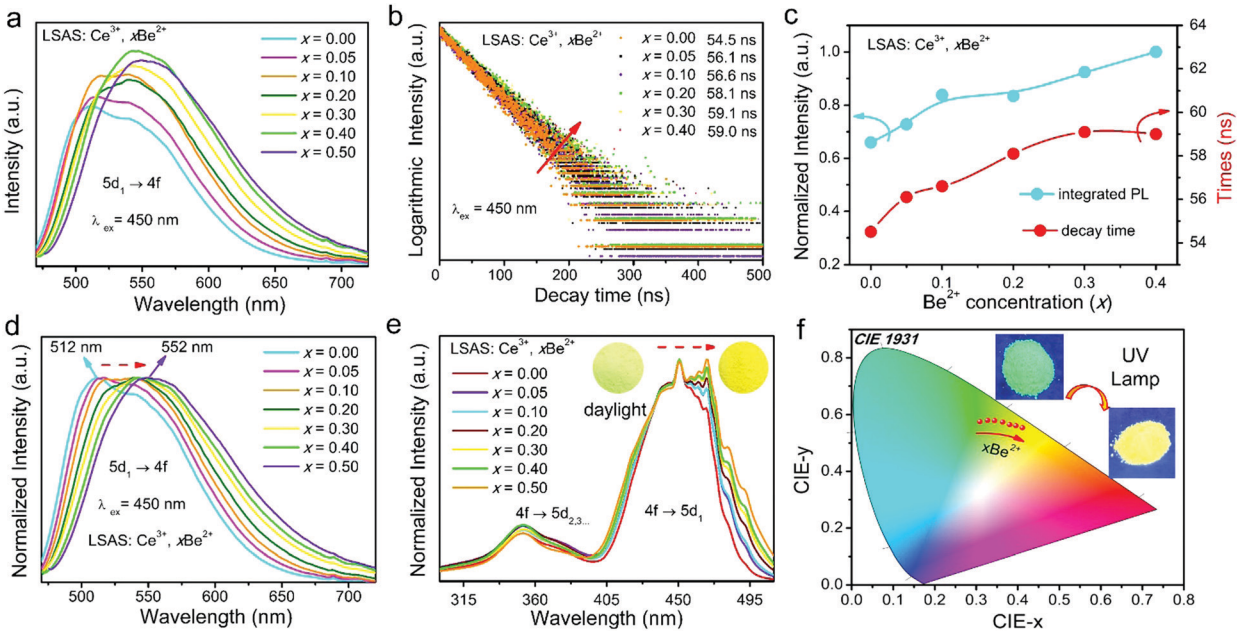

Fig. 2 Be^{2+} concentration-dependent room temperature (a) PL emission spectra (λ_{ex} = 450 nm) and (b) PL decay curves from the 5d state of Ce^{3+} in LSAS:Ce,*x*Be by monitoring the Ce^{3+} maximum emission peak. (c) The dependence of the normalized integrated PL intensity and decay lifetime on Be^{2+} concentration (*x*) in LSAS:Ce,*x*Be. (d), (e) Normalized PL and PLE spectra of LSAS:Ce,*x*Be. (f) CIE (*x*, *y*) coordinates of LSAS:Ce,*x*Be showing continuous tuning of emission colors from green to yellow with increasing doping content of Be^{2+}. The insets in (e) and (f) show photographs of samples taken in daylight and under a 365 nm UV lamp.

also conforms to the Pauling prediction that the coordination number of Be^{2+} is four.[21] Due to Al^{3+} and Si^{4+} ions randomly sharing the same site with an occupancy ratio of 2 : 1, we propose that Be^{2+} could substitute both Al^{3+} and Si^{4+} with a substitution ratio of Be^{2+} for Al^{3+} of 2/3 and for Si^{4+} of 1/3. To maintain charge neutrality, the Si^{4+}/Al^{3+} anti-site substitution model is proposed and verified as reasonable in the aluminosilicate system, with a charge balance equation of $2Al^{3+} = Be^{2+} + Si^{4+}$ ($3Be^{2+} + 4Si^{4+} = Si^{4+} + 2Al^{3+} + 4Al^{3+}$), and a similar model has been found in other systems.[33]

We then performed steady- and transient-state spectroscopic studies on the Be^{2+}-free and -doped LSAS:Ce phosphors to compare their luminescence properties. Fig. 2a shows the PL spectra of LSAS:Ce,*x*Be (x = 0.00–0.50) with different Be^{2+} doping concentrations. Under 450 nm blue light excitation, all the phosphors exhibit a broad emission band corresponding to the electronic transitions from the lowest T_{2g} level of the 5d state to the $^2F_{5/2}$ and $^2F_{7/2}$ levels of the 4f ground state of Ce^{3+}. Importantly, the integrated PL intensities of these Be^{2+}-doped phosphors show improved emission intensities compared with their Be^{2+}-free counterpart (Fig. 2c). Accordingly, the internal/external quantum efficiencies of the phosphors increase from 79.2%/26.7% (x = 0.00) to 84.5%/32.9% (x = 0.40) (Table S4, ESI†). The luminescent decay curves measured under 450 nm pulse light excitation are shown in Fig. 2b. Evidently, they all exhibit a single exponential decay behavior, with PL lifetimes increasing from 54.5 to 59.1 ns, depending on the increasing Be^{2+} content (Fig. 2b and c). The enhanced emission intensity/efficiency and prolonged PL lifetimes are strong confirmation that Be^{2+} doping can effectively suppress the nonradiative relaxation processes and thus enhance emission intensities. Due to the strong covalent bonding between Be^{2+} and its ligand, O^{2-}, which is comparable to Al– and Si–ligand bonds,[23] and the decreased formal charge, the Be^{2+} ions substituted for tetrahedrally coordinated Al_2/Si_2 ions at the second coordination sphere of Ce^{3+}, as shown in Fig. 3a, can form a more stable and rigid local covalent environment around Ce^{3+}. Thus, Be-containing LSAS garnet has a higher degree of rigid network compared with LSAS, and so is more ideal for high efficiency emisison.

Fig. 2d and e demonstrate the normalized PL and PLE spectra recorded at room temperature, in which both spectra show red shifting and inhomogeneous broadening behavior with increasing Be^{2+} doping concentrations. The maximum emission peak is shifted from 512 (x = 0.00) to 552 nm (x = 0.50) and the emission colors change from green to yellow, as shown in the Commission Internationale de L'Eclairage (CIE) chromaticity diagram (Fig. 2f) and CIE data (Table S5, ESI†). The digital photographs taken under 365 nm UV lamp irradiation (inset in Fig. 2f) clearly demonstrate the tunable emission colors. The body colors of the phosphors also change from yellow green to vivid yellow (inset in Fig. 2e), due to the broadening and red shift of the Ce^{3+} 4f → $5d_1$ electronic transition at ~450 nm in the PLE spectra. The broadening effect in the PL/PLE spectrum is generally related to enhanced electron–lattice interactions or fluctuations in the local Ce^{3+} coordination sphere. Since the first cause can be excluded according to the analysis given above, the spectrum broadening is attributed to the latter; namely, mixed (Al, Si, and Be) occupation

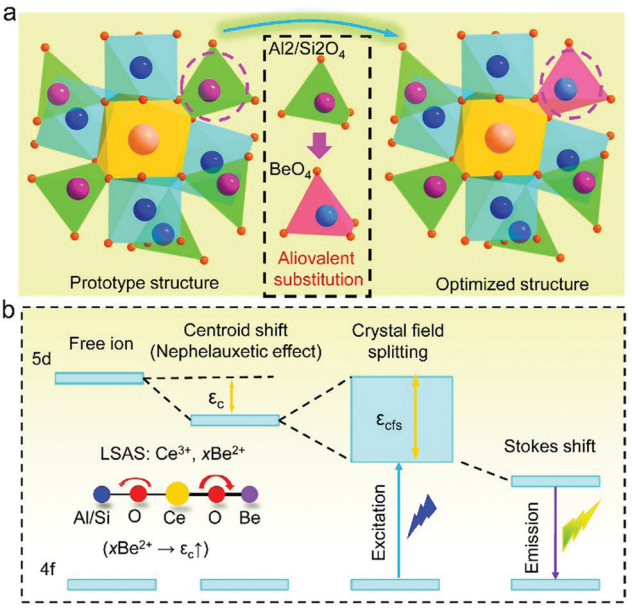

Fig. 3 (a) Schematic illustration of aliovalent substitution in the local framework of the Lu/Sr/CeO_8 dodecahedron. (b) Schematic energy level diagram for Ce^{3+} ions in the LSAS host crystal structure.

leads to a range of chemically differing second coordination spheres around Ce^{3+}. As the maximum spectral peaks shift to the less energetic region, they are generally associated with increased crystal field splitting (ε_{cfs}) or centroid shift (ε_c), as shown in Fig. 3b. The CeO_8 coordination polyhedron distortion index (D) can be used to analyze ε_{cfs}:[34]

$$D = \frac{1}{n}\sum_{i=1}^{n}\frac{|l_i - l_{av}|}{l_{av}} \quad (1)$$

where l_i is the distance from the center atom to the ith coordinating atom, l_{av} is the average bond length, and n is the total number of Ce–O bonds. The calculated D are 0.020, 0.022 and 0.026 for x equal to 0.00, 0.20 and 0.40, respectively, and increase linearly with Be^{2+} concentration. Therefore, Be^{2+} doping can result in an enhanced ε_{cfs} and lead to the spectral red shift. As a comparison, the ε_c of Ce^{3+} 5d orbitals, which is mainly affected by the host composition, can be qualitatively analyzed by the model developed by Dorenbos. The relationship between ε_c and the anion spectroscopic polarizability α_{sp} is given by:[35]

$$\varepsilon_c = 1.79 \times 10^{13}\alpha_{sp}\sum_{i=1}^{N}\frac{1}{(R_i - 0.6\Delta R)^6} \quad (2)$$

where R_i is the individual bond length to the N coordinating anions in the unrelaxed lattice. $\Delta R = R_M - R_{Ln}$, where R_M is the ionic radius of the cation that is replaced by the lanthanide (Ln) with ionic radius R_{Ln} and $0.6\Delta R$ is an estimation of the bond length relaxation. A qualitative relationship between α_{sp} and the average cation electronegativity, χ_{av}, in oxide compounds is defined as:[35]

$$\alpha_{sp} = 0.4 + \frac{4.6}{\chi_{av}^{\ 2}} \quad (3)$$

The average cation electronegativity, χ_{av}, can be calculated by the following equation:[36]

$$\chi_{av} = \frac{1}{N_a}\sum_{i}^{N_c}\frac{z_i\chi_i}{\gamma} \quad (4)$$

where the summation is over all cations (N_c) in the formula of the compound, and N_a is the number of anions in the formula. A cation of formal charge $+z_i$ will bind, on average, with z_i/γ anions of formal charge $-\gamma$. The χ_{av} values were determined to be 1.52, 1.49, and 1.47 for x equal to 0.00, 0.20 and 0.40, respectively, and the a_{sp} values were 2.39, 2.47, 2.53. According to eqn (2), it can be seen that ε_c is positively related to a_{sp}. Therefore, a higher Be^{2+} concentration results in an enhanced ε_c, which is also in line with the lower inductive effect of Be^{2+} in comparison with Al/Si, and thus leads to a more distinct nephalauxetic effect. To summarize, the observed PLE/PL spectral red shift in Be^{2+}-doped LSAS:Ce is governed by the increased crystal field splitting and centroid shift induced by the aliovalent substitution of Be^{2+}.

Another key advantage of adopting Be^{2+} to tune phosphor properties is that the thermal quenching temperature is expected to remain high, as confirmed by the temperature-dependent emission spectra (Fig. S2, ESI†) and the temperature-dependent normalized emission spectra (Fig. 4a). Compared with LSAS:Ce showing zero thermal quenching (103% at 210 °C of the integrated emission intensity at 30 °C), there is only a tiny decrease in thermally stable behavior among Be^{2+}-doped LSAS:Ce (97% at 210 °C and 92% at 210 °C for 20% and 40% Be^{2+} concentrations, respectively), suggesting that Be^{2+} can maintain the phosphors with good thermally stable PL. The origin of the excellent thermal PL in LSAS:Ce,xBe is also related to its rigid crystal structure. The Raman spectra of LSAS:Ce,xBe (x = 0.00, 0.20, and 0.40) were recorded to further understand the rigidity of the structure, as shown in Fig. S3 (ESI†). The modes in the range of 450–700 cm^{-1} are assigned to bending motions of the $(Al,Si)O_4$ tetrahedra, and the high frequency modes (800–1100 cm^{-1}) are related to symmetric and asymmetric internal stretching vibrations of rigid $(Al,Si)O_4$ tetrahedra.[37] The Raman peaks remain identical when the Be^{2+} concentration increases, indicating that the phosphors maintain the LSAS garnet structure, as shown by XRD. Furthermore, all peaks in the Be^{2+}-doped samples are narrow and sharp, as in the non-doped samples, indicating highly rigid structures despite Be^{2+} doping. The thermally stable PL for LSAS:Ce,xBe can also be specifically explained by the configurational coordinate diagram in Fig. 4b. As shown in the figure, the larger offset ΔR values between the 4f and 5d parabolas, mean that the excited electrons in the 5d state at elevated temperature can more easily overcome the ΔE energy barrier, leading to a more severe thermal quenching.[38] In the present case, due to the rigid crystal structures, the large offset ΔR is prevented and, therefore, high thermally stable PL is achieved. For Be^{2+}-doped samples, the Ce^{3+} 5d parabolas are vertically displaced with increasing Be^{2+} ratio based on the PLE/PL spectra, resulting in an insignificantly narrowed ΔE, and therefore only a tiny decrease in the thermal stablility of the PL is observed.

Finally, to evaluate whether the composition-optimized phosphor has promise for practical applications, prototype WLED devices were fabricated by combining a 450–460 nm blue chip with LSAS:Ce (LED-S1), LSAS:Ce,0.40Be (LED-1) as well as a mixture of LSAS:Ce,0.40Be and commercial $CaAlSiN_3:Eu^{2+}$ red phosphor (LED-2). The emission spectra and the CIE chromaticity coordinates of these WLEDs driven at 20 mA current are shown in Fig. 5a–c and Fig. S4 (ESI†), and some important photometric and chromaticity parameters are also noted in these figures. The LED-S1 obtains a cool white light with a high CCT of 26 960 K, color rendering index (R_a) of 66.7, CIE coordinate of (0.229, 0.271), and luminous efficiency (LE) of 133.5 lm W^{-1}. Meanwhile, LED-1 gives performance parameters of CCT = 8773 K, R_a = 70, CIE coordinate (0.282, 0.313) and a high LE = 167 lm W^{-1}, which is much better than LED-S1 mainly due to the enhanced emission intensity/efficiency and emission spectra of LSAS:Ce,0.40Be compared with those of LSAS:Ce. Furthermore, by adding $CaAlSiN_3:Eu^{2+}$ red phosphor, a high-quality warm LED-2 with improved overall performance of

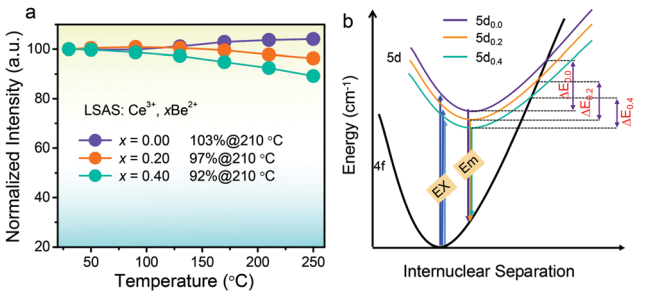

Fig. 4 (a) Temperature-dependent normalized emission spectra of three representative LSAS:Ce,xBe (x = 0.00, 0.20, and 0.40) samples. (b) The schematic configurational coordinated diagram of the thermal quenching mechanism.

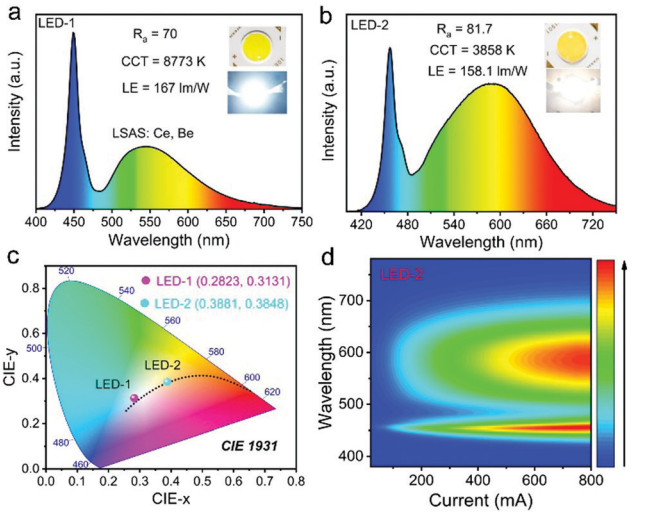

Fig. 5 Emission spectra of WLED devices fabricated by yellow LSAS:Ce,0.40Be (a) without and (b) with commercial $CaAlSiN_3:Eu^{2+}$ red phosphor. The inset shows the photographs of their corresponding LEDs. (c) CIE color coordinates of the fabricated WLEDs. (d) Current-dependent emission spectra of WLED-2 in the current range 20–800 mA.

CCT = 3858 K, R_a = 81.7, CIE coordinate (0.388, 0.385), and LE = 158.1 lm W^{-1} was also fabricated. Fig. 5d and Fig. S4b (ESI†) give the emission spectra of LED-2 operating under different driving currents, and it can be seen that, with a current increase from 20 to 800 mA, the luminescence intensity of the device continuously increases. Compared with 20 mA, the integratated photoluminescence intensity of the device driven at 800 mA is 24-fold larger. Moreover, the luminous efficiencies of the device driven at 350 mA and 800 mA are as high as 104.8 lm W^{-1} and 64.5 lm W^{-1}, respectively (Table S6, ESI†). The CIE coordinates are found to be only slightly blue shifted, from (0.388, 0.385) to (0.377, 0.370), with a variation of Δx and Δy of just 0.011 and 0.015 (Fig. S4c, ESI†), respectively. All these findings demonstrate the excellent color stability of the device and the hope that they can be applied in high-powered light applications.

4. Conclusions

In summary, we successfully developed a new aliovalent substitution strategy to optimize LED phosphor performance by intentional incorporation of Be^{2+} ions into a tetrahedral site of an aluminosilicate-based garnet phosphor, which allows crystal-structure optimization to improve and modify luminescence. As exemplified by the Be^{2+}-doped $Lu_2SrAl_4SiO_{12}$:Ce^{3+} garnet, the modified samples shows tunable emission colors, enhanced emission intensity/efficiency and the desired thermally stable photoluminescence for LED applications. The Be^{2+} ion incorporates into the Al_2/Si_2O_4 tetrahedron at the second coordination sphere of Ce^{3+}, providing more robust surroundings around Ce^{3+} and thus enhancing the emission. A prototype LED device made by using the as-fabricated $Lu_2SrAl_4SiO_{12}$:Ce^{3+},Be^{2+} shows a high luminous efficiency of 158 lm W^{-1}, low correlated color temperature of 3858 K and high color rendering index of 81.7, demonstrating that with incorporation of the Be^{2+} ion the phosphors can optimize the optical performance of WLED devices. Our theoretical and experimental studies described here will help to guide the discovery of rigid covalent compounds with further reinforced structural rigidity *via* aliovalent substitution and allow for the creation of good LED phosphors with high quantum efficiency, improved thermal stability and controllable excitation/emission properties.

Conflicts of interest

The authors declare no conflicts of interest.

Acknowledgements

This work was supported by the National Natural Science Foundation of China (No. 51722202 and 51972118), the Guangdong Provincial Science & Technology Project (2018A050506004) and the Fundamental Research Funds for the Central Universities (D2190980).

References

1 H. A. Höppe, *Angew. Chem., Int. Ed.*, 2009, **48**, 3572–3582.
2 Z. G. Xia and Q. L. Liu, *Prog. Mater. Sci.*, 2016, **84**, 59–117.
3 P. Pust, P. J. Schmidt and W. Schnick, *Nat. Mater.*, 2015, **14**, 454–458.
4 M. Zhao, H. X. Liao, L. X. Ning, Q. Y. Zhang, Q. L. Liu and Z. G. Xia, *Adv. Mater.*, 2018, **30**, 1802489.
5 H. Lin, T. Hu, Y. Cheng, M. X. Chen and Y. S. Wang, *Laser Photonics Rev.*, 2018, **12**, 1700344.
6 M. H. Fang, Y. T. Tsai, H. S. Sheu, J. F. Lee and R. S. Liu, *J. Mater. Chem. C*, 2018, **6**, 10174–10178.
7 V. Rajendran, H. Chang and R. S. Liu, *Opt. Mater. X*, 2019, 100011.
8 Y. H. Kim, P. Arunkumar, B. Y. Kim, S. Unithrattil, E. Kim, S. H. Moon, J. Y. Hyun, K. H. Kim, D. Lee, J. S. Lee and W. B. Im, *Nat. Mater.*, 2017, **16**, 543–550.
9 J. W. Qiao, L. X. Ning, M. S. Molokeev, Y.-C. Chuang, Q. L. Liu and Z. G. Xia, *J. Am. Chem. Soc.*, 2018, **140**, 9730–9736.
10 B. Q. Shao, J. S. Huo and H. P. You, *Adv. Opt. Mater.*, 2019, 1900319.
11 Z. G. Xia, C. G. Ma, M. S. Molokeev, Q. L. Liu, K. Rickert and K. R. Poeppelmeier, *J. Am. Chem. Soc.*, 2015, **137**, 12494–12497.
12 Y. Wei, G. C. Xing, K. Liu, G. G. Li, P. P. Dang, S. S. Liang, M. Liu, Z. Y. Cheng, D. Y. Jin and J. Lin, *Light: Sci. Appl.*, 2019, **8**, 15.
13 M. H. Fang, S. Y. Meng, N. Majewska, T. Leśniewski, S. Mahlik, M. Grinberg, H. S. Sheu and R. S. Liu, *Chem. Mater.*, 2019, **31**, 4614.
14 H. H. Zhang, Y. Y. Chen, X. Y. Zhu, H. C. Zhou, Y. Yao and X. D. Li, *J. Lumin.*, 2019, **207**, 477–481.
15 Z. Wang, J. Ha, Y. H. Kim, W. B. Im, J. McKittrick and S. P. Ong, *Joule*, 2018, **2**, 914–926.
16 Y. Zhuo, A. M. Tehrani, A. O. Oliynyk, A. C. Duke and J. Brgoch, *Nat. Commun.*, 2018, **9**, 4377.
17 A. C. Duke, S. Hariyani and J. Brgoch, *Chem. Mater.*, 2018, **30**, 2668–2675.
18 J. Brgoch, S. P. DenBaars and R. Seshadri, *J. Phys. Chem. C*, 2013, **117**, 17955–17959.
19 K. A. Denault, J. Brgoch, S. D. Kloß, M. W. Gaultois, J. Siewenie, K. Page and R. Seshadri, *ACS Appl. Mater. Interfaces*, 2015, **7**, 7264–7272.
20 K. A. Denault, J. Brgoch, M. W. Gaultois, A. Mikhailovsky, R. Petry, H. Winkler, S. P. DenBaars and R. Seshadri, *Chem. Mater.*, 2014, **26**, 2275–2282.
21 L. Pauling, *J. Am. Chem. Soc.*, 1929, **51**, 1010–1026.
22 Y. G. Chen, M. L. Xing, Y. Guo, Z. S. Lin, X. J. Fan and X. M. Zhang, *Inorg. Chem.*, 2019, **58**, 2201–2207.
23 P. Strobel, C. Maak, V. Weiler, P. J. Schmidt and W. Schnick, *Angew. Chem., Int. Ed.*, 2018, **57**, 8739–8743.
24 P. Strobel, R. Niklaus, P. J. Schmidt and W. Schnick, *Chem. – Eur. J.*, 2018, **24**, 12678–12685.
25 P. Strobel, T. de Boer, V. Weiler, P. J. Schmidt, A. Moewes and W. Schnick, *Chem. Mater.*, 2018, **30**, 3122–3130.

26 E. Elzer, R. Niklaus, P. J. Strobel, V. Weiler, P. J. Schmidt and W. Schnick, *Chem. Mater.*, 2019, **31**, 3174–3182.
27 Bruker AXS TOPAS V4, *General profile and structure analysis software for powder diffraction data. – User's Manual*, Bruker AXS, Karlsruhe, Germany, 2008.
28 Z. G. Xia and A. Meijerink, *Chem. Soc. Rev.*, 2017, **46**, 275–299.
29 J. Ueda and S. Tanabe, *Opt. Mater. X*, 2019, 100018.
30 Y. Xiao, W. Xiao, L. Zhang, Z. Hao, G. H. Pan, Y. Yang, X. Zhang and J. Zhang, *J. Mater. Chem. C*, 2018, **6**, 12159–12163.
31 H. S. Yoder and M. L. Keith, *Am. Mineral.*, 1951, **36**, 519–533.
32 W. Zachariasen, *Nor. Geol. Tidsskr.*, 1925, **8**, 189–200.
33 M. Zhao, Z. G. Xia, X. X. Huang, L. X. Ning, R. Gautier, M. S. Molokeev, Y. Y. Zhou, Y.-C. Chuang, Q. Y. Zhang, Q. L. Liu and K. R. Poeppelmeier, *Sci. Adv.*, 2019, **5**, eaav0363.
34 W. H. Baur, *Acta Crystallogr., Sect. B: Struct. Crystallogr. Cryst. Chem.*, 1974, **30**, 1195–1215.
35 P. Dorenbos, *J. Lumin.*, 2013, **135**, 93–104.
36 P. Dorenbos, *Phys. Rev. B: Condens. Matter Mater. Phys.*, 2002, **65**, 235110.
37 Y. F. Wu, Y. H. Chan, Y. T. Nien and I. G. Chen, *J. Am. Ceram. Soc.*, 2013, **96**, 234–240.
38 Y. Wang, J. Ding, Y. Wang, X. Zhou, Y. Cao, B. Ma, J. Li, X. Wang, T. Seto and Z. Zhao, *J. Mater. Chem. C*, 2019, **7**, 1792–1820.

